



# High-quality AlGaN epitaxy on lattice-engineerable AlN template for high-power UVC light-emitting diodes



Sebastian Walde<sup>a</sup>, Cheng-Yao Huang<sup>b</sup>, Chia-Lung Tsai<sup>c</sup>, Wen-Hsuan Hsieh<sup>d</sup>, Yi-Keng Fu<sup>c</sup>, Sylvia Hagedorn<sup>a</sup>, Hung-Wei Yen<sup>b</sup>, Tien-Chang Lu<sup>d</sup>, Markus Weyers<sup>a</sup>, Chia-Yen Huang<sup>c,d,\*</sup>

<sup>a</sup> Ferdinand-Braun-Institut gGmbH, Leibniz-Institut fuer Hochfrequenztechnik, Gustav-Kirchhoff-Strasse 4, Berlin 12489, Germany

<sup>b</sup> Department of Materials Science and Engineering, National Taiwan University, No. 1, Sec. 4, Roosevelt Road, Taipei, Taiwan ROC

<sup>c</sup> Electronic and Optoelectronic System Research Laboratories, Industrial Technology Research Institute, 195, Sec.4, Chung Hsing Rd., Hsinchu, Taiwan ROC

<sup>d</sup> Department of Photonics, College of Electrical and Computer Engineering, National Yang Ming Chiao Tung University, Hsinchu 30010, Taiwan ROC

## ARTICLE INFO

### Article history:

Received 6 October 2021

Revised 25 December 2021

Accepted 4 January 2022

Available online 6 January 2022

## ABSTRACT

AlGaN-based UVC light-emitting diodes (LED) were fabricated on high-quality AlN templates with an engineerable in-plane lattice constant. The controllability of the in-plane strain originated from the vacancy formation in Si-doped AlN (AlN:Si) and their interaction with edge dislocations. The strain state of the Si:AlN top interface could be well depicted by a dislocation-tilt model depending on the buffer strain state, threading dislocation density (TDD), and regrown Si:AlN thickness. The validity of the model was verified by cross-sectional TEM analysis. With a gradually widened lattice constant of regrown Si:AlN layer, strain-induced defects of subsequently grown n-AlGaN was suppressed. Therefore, growing a current spreading layer which possesses a moderate Al content (<65%), decent thickness (>1.5 μm), and a low TDD (<1.0 × 10<sup>9</sup> cm<sup>-2</sup>) simultaneously becomes possible. Additionally, the idea of an optimal edge TDD ( $\rho_{e,opt}$ ) in the AlN buffer was revealed for growing high-quality n-AlGaN layers with a targeted thickness. After a deliberate strain-TDD engineering for Si:AlN and n-AlGaN, high-power UVC LEDs ( $\lambda = 275$  nm,  $P > 200$  mW) with a low forward voltage ( $V_f = 5.7$  volt) were demonstrated at  $I = 1.35$  A. The low forward voltage under high current injection density was attributed to the success in preparation of a low series resistance and high-quality n-AlGaN current spreading layer.

© 2022 Acta Materialia Inc. Published by Elsevier Ltd. All rights reserved.

## 1. Introduction

AlGaN-based light-emitting diodes (LED) in the UVC spectral region ( $\lambda = 200\text{--}280$  nm) are promising devices for the next-generation of sterilization and disinfection applications [1–4]. Although the external quantum efficiency (EQE) and wall-plug efficiency (WPE) of AlGaN-based UVC LEDs still have much room for improvement, they start to enter the consumer market due to their inherent advantages of compact size, fast turn-on, and environmental friendliness. The possibility of fast disinfection of personal protective equipment and environmental sterilization with UVC light modules have been intensely explored during the COVID-19 pandemic [5–10]. Studies also revealed that SARS-COV-2 virus can be efficiently inactivated by a high flux of UVC light irradiation. Liu et al. utilized a 15 × 13 UVC LED array to disinfect SARS-COV-2 samples within one second [10]. To achieve the same dosage

of UVC radiation with less LED chips, one might either enhance the EQE of the LEDs or operate them under higher injection current. The state-of-the-art UVC-LED EQE has increased up to 20% after incorporating different light extraction efficiency improvement techniques such as nano-patterned sapphire substrates, transparent p-AlGaN contact layer and UV-transparent resin packaging [11]. However, the high forward voltage ( $V_f = 16$  V under  $I = 20$  mA) hampered the high-power applications. The high forward voltage was attributed to the extremely challenging electrical contacts on p-AlGaN layers. To date, the forward voltage of UVC-LEDs with p-AlGaN contacts ranges from 8 to 50 V regardless of the injection current level and electrode materials [11–16]. With such high forward voltage, one might obtain a benchmark EQE under low injection current, but the final output power from a single chip is still limited. The strong accompanying Joule heating also imposes difficulties in thermal management for packaging. As a result, UVC LEDs with p-GaN contact layer remain mainstream unless a new breakthrough in p-AlGaN contact technology occurs.

Improving the internal quantum efficiency (IQE) by a better quality of the AlN template is also a great interest in research.

\* Corresponding author at: Electronic and Optoelectronic System Research Laboratories, Industrial Technology Research Institute, 195, Sec.4, Chung Hsing Rd., Hsinchu, Taiwan ROC.

E-mail address: [cyhuang06@nycu.edu.tw](mailto:cyhuang06@nycu.edu.tw) (C.-Y. Huang).

The threading dislocation density (TDD) of AlN layers is usually assessed by the full-width at half-maximum (FWHM) of the X-ray rocking curves (XRC) of the 002 and 102 reflections (or the 002/102 FWHM). The densities of dislocations with screw or edge component can be extracted from the 002 and 102 FWHMs as in reference [17]. The accuracy of the model was verified by plan-view transmission electron microscopy, defect selective etching and counting dark-spots in cathodoluminescence images [18–20]. In most reported cases, the edge dislocations dominated the AlN template quality. According to the theoretical model, the IQE of AlGaN quantum wells is less than 10% if the TDD is  $2 \times 10^9 \text{ cm}^{-2}$ , which corresponds to 002/102 FWHM of around 100/450 arcsec [21]. In early development, the quality of AlN templates on sapphire was improved by growth parameter modulation in metalorganic vapor phase epitaxy (MOVPE) [22–24]. Growing AlN on nPSS allows to terminate threading dislocations (TDs) via lateral growth and film coalescence [25–28]. However, the AlN quality improvement via above techniques faces challenges like film cracking, low wafer throughput, or complicated growth procedures. Miyake et al. proposed high-temperature annealing (HTA) to significantly reduce the TDD of pre-deposited AlN buffer layers and simplify the regrowth process of AlN [29–32]. The buffer deposition method could be MOVPE, sputtering, or hydride vapor phase epitaxy (HVPE), and it can be applied on flat sapphire substrate (FSS) along various orientations as well as nPSS [27,33–35]. State-of-the-art 102 FWHM of AlN was reported to be less than 150 arcsec after multiple HTA [32]. The functionality and versatility of HTA technologies attracted much attention. Although AlN quality improvement by HTA was intensively studied, reports of actual LED device performance improvements are scarce. The 002 and 102 FWHM of AlGaN epitaxy on HTA AlN buffers was rarely discussed neither. For example, Susilo et al. demonstrated 265 nm UVC LEDs on HTA-AlN [36,20]. The EQE after lens packaging reached 3.6% at  $I = 50 \text{ mA}$ , and 2.9% at  $I = 350 \text{ mA}$ , which gave the maximum output power of 47 mW under 350 mA current injection. The forward voltages ( $V_f$ ) increased from 6 V to 13 V when current was increased from 50 mA to 350 mA, and the WPE dropped from 2.8 to 1.0%. The significant deterioration of EQE and WPE with increasing injection current could be attributed to self-heating due to the large series resistance ( $R_s$ ). Part of the high  $R_s$  stems from the design trilemma between the alloy composition, total thickness, and the crystalline quality of the n-AlGaN current spreading layers. The ideal n-AlGaN shall have a moderate Al content, a sufficient thickness, and a low TDD to suppress non-radiative recombination and to lower the forward voltage simultaneously. As the Al mole fraction of AlGaN increases from 70 to 100%, the maximum available carrier density ( $n_{\max}$ ) degrades drastically due to the high activation energy ( $E_a$ ) of the Si dopant and the self-compensation by parasitic vacancy-related point defects [4,37–39]. According to theoretical calculation by Harris et al.,  $n_{\max}$  is below  $1 \times 10^{16} \text{ cm}^{-3}$  for Si-doped AlN [37]. Due to the high  $E_a$  and low  $n_{\max}$ , decent n-contacts and current spreading become critical for Al content above 70% in n-AlGaN. Therefore, a moderate Al content in n-AlGaN electron injection layer is desired for improving the WPE and the droop behavior of UVC LEDs. Unfortunately, the capability of growing a thick n-AlGaN with moderate Al content is strongly limited by its lattice mismatch to the AlN template. High compressive strain in AlGaN eventually results in a low critical layer thickness through which new dislocations would nucleate. The nucleation of new dislocations in AlGaN will be promoted if pre-existing dislocations fail to accommodate the mismatch strain. Therefore, the TDD of a micrometer-thick n-AlGaN grown on low TDD AlN templates was often still high [40,41]. For example, Y. Kawase et al. directly grew  $\text{Al}_{0.55}\text{Ga}_{0.45}\text{N}$  on HTA-AlN with 3D-2D growth mode transition to fully relax the strain. However, the TDD of 1  $\mu\text{m}$  AlGaN layer was above  $3.0 \times 10^9 \text{ cm}^{-2}$ , which makes the

purpose of using high-quality AlN buffers questionable [40]. A design trilemma among the composition, thickness and the TDD of n-AlGaN layer exists. However, such design trilemma was rarely discussed. Huang et al. firstly demonstrated strain relaxation by introduction of high Si-doping to the AlN template [41]. However, the strain relaxation mechanism was not explained with details. In this report, we demonstrate that the strain state of the AlN templates can be actively engineered by the thickness of the regrown AlN:Si. We also revealed the concept of the “optimal initial threading dislocation density” for growing high-power UVC LEDs. It suggests that we shall not pursue AlN templates with a TDD as low as possible. A low forward-voltage ( $V_f = 5.6 \text{ V}$ ) UVC LED ( $\lambda = 275 \text{ nm}$ ) with a high output power under  $I = 1.35 \text{ A}$  was demonstrated as the proof of the importance for deliberate strain engineering.

## 2. Method

The AlN/AlGaN epitaxial process was conducted in an MOVPE system (TNSC SR-4000) on AlN/sapphire templates with a thickness of  $0.31 \pm 0.03 \text{ } \mu\text{m}$  grown by HVPE. Conventional trimethylaluminum, trimethylgallium,  $\text{NH}_3$ , and  $\text{SiH}_4$  were used as the precursors in MOVPE. Both Si:AlN and n-AlGaN were grown under  $\text{H}_2$  ambient. Prior to the introduction of the precursors, the HVPE AlN template was baked in the MOVPE system under  $\text{H}_2$  for 30 min at growth temperature of the Si:AlN. The growth temperature of the Si:AlN was  $1220^\circ\text{C}$  under a pressure of  $P = 10 \text{ kPa}$ . The V/III ratio was around 530 and the growth rate of Si:AlN was  $0.9 \text{ } \mu\text{m}\cdot\text{h}^{-1}$ . The Si-concentration [Si] in Si:AlN was  $2.0 \times 10^{19} \text{ cm}^{-3}$ . With a high-quality HVPE buffer, the crystal quality of Si:AlN is rather robust to the growth conditions. The crystal quality of Si:AlN does not show significant variation on growth temperature from  $1200$  to  $1240^\circ\text{C}$ , and on growth rate from  $0.6 \text{ } \mu\text{m}\cdot\text{h}^{-1}$  to  $1.2 \text{ } \mu\text{m}\cdot\text{h}^{-1}$ . The growth temperature and growth rate of n-AlGaN was  $1080^\circ\text{C}$  and  $0.6 \text{ } \mu\text{m}\cdot\text{h}^{-1}$ , respectively.

The buffer and n-AlGaN epitaxy were analyzed by high-resolution X-ray diffractometer (HR-XRD). 002/102  $\omega$ -scans, fine-scale 002  $\omega$ - $2\theta$  scans were conducted in a Malvern Panalytical X'Pert3 system with a four-fold 220 Ge monochromator and a  $0.5 \times 5 \text{ mm}^2$  aperture before the light source ( $\text{Cu-K}\alpha 1$ ) and a triple axis configuration on the detector side. To depict XRD reciprocal space maps, a PIXcel3D array detector was used. The lattice constant, strain states and alloy composition of each layer were extracted from HR-XRD measurements. Parameter extraction from the HR-XRD measurements is explained in the supporting information.

A field-emission gun transmission electron microscope (FEI TECNAI G2 F20) was used to determine the characteristics of dislocations in the materials. The TEM samples were prepared by lift-out technique with a focused ion beam system (FEI Helios Nanolab 600i). The dislocation inclination angle was evaluated from exact-zone DF images. The type of dislocation was determined by weak beam dark-field images under two-beam condition.

Full UVC LED wafer was fabricated into  $1.07 \times 1.07 \text{ mm}^2$  (or  $42 \times 42 \text{ mil}^2$ ) flip-chips. The LED epilayer structure is analogue to those in reference [16], but the growth conditions were further optimized. The p-contact layer consists of 80 nm p-GaN with conventional indium-tin oxide (ITO) electrode. The [Mg] in p-GaN was estimated to be  $4.0 \times 10^{19} \text{ cm}^{-2}$ . The n-electrode was made of a Ti/Al/Ni/Au multilayer on n- $\text{Al}_{0.63}\text{Ga}_{0.37}\text{N}$ . [Si] in n-AlGaN was  $2.5 \times 10^{19} \text{ cm}^{-3}$ . A  $\text{SiO}_2$ -based lens was bonded to the flip-chip for LEE enhancement. Flip-chips were bonded on a  $3.5 \times 3.5 \text{ mm}^2$  ceramic sub-mount with AuSn. The submount was fixed on a metal stage designed for the Teflon-coated integrated sphere. Although the stage worked as a heat reservoir, the temperature of the stage was not controlled externally. The integration time for each point

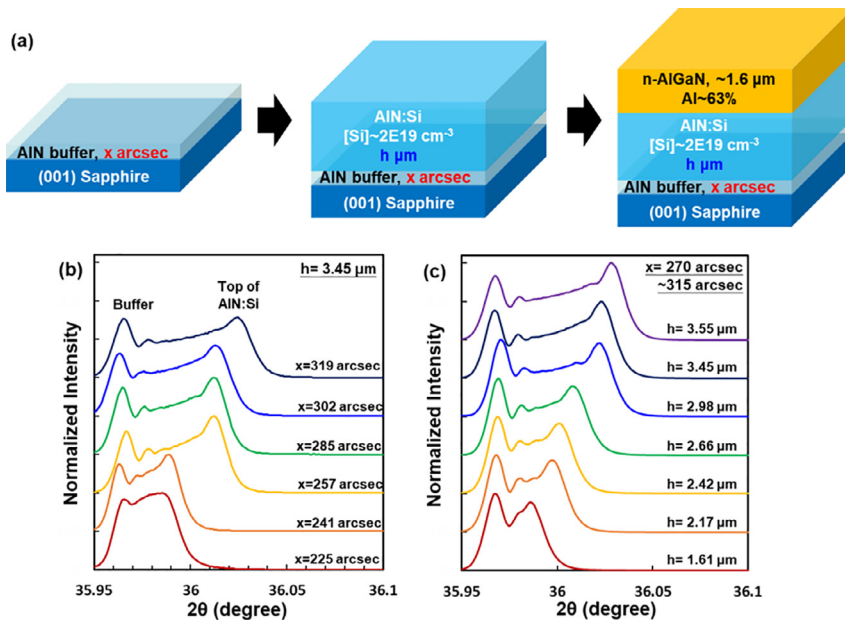


**Fig. 1.** (a) Schematic epilayer structure of n-AlGaN on AlN:Si. XRD 002  $\omega$ -2 $\theta$  fine-scan of the AlN/Si:AlN layer of samples (b) with the same Si:AlN thickness  $h$ , but a broad range of 102 FWHMs in the buffer  $x$ ; (c) with similar 102 FWHMs in buffer  $x$ , but varying thickness  $h$  the AlN:Si. The  $\omega$ -2 $\theta$  scans were normalized and vertically shifted for image clarity.

in Fig. 6 was 10 ms under DC injection. The width of DC continuous injection was also 10 ms.

### 3. Results and discussion

#### 3.1. AlN template with an engineerable lattice constant

HVPE AlN buffers on sapphire were first overgrown with Si:AlN layers and then with 1.6 μm n-AlGaN layers by MOVPE as illustrated in Fig. 1(a). The epitaxial growth parameters of Si:AlN and n-AlGaN were identical, but the initial buffer quality and the regrown thickness of the Si-doped AlN varied. The 102 FWHMs of the buffer are denoted as  $x$  and the Si:AlN thickness as  $h$ . According to secondary ion mass spectrometry measurements, the Si-concentration [Si] in Si:AlN and n-AlGaN was  $2.0 \times 10^{19} \text{ cm}^{-3}$  and  $2.5 \times 10^{19} \text{ cm}^{-3}$ , respectively. In series A,  $x$  varied from 225 arcsec to 319 arcsec while the thickness was kept constant at  $h = 3.45 \mu\text{m}$ . Series B had a closer distribution of  $x$ , but  $h$  ranged from 1.61 μm to 3.55 μm. In Fig. 1(b) and (c) the  $\omega$ -2 $\theta$  fine-scans of the 002 reflection of the AlN layers are shown. Two peaks are observed in all samples. The peak with the lower 2 $\theta$  value refers to the HVPE buffer while the other one at higher 2 $\theta$  value represents the top interface of the Si:AlN layer. The out-of-plane lattice constant of the HVPE buffer and Si:AlN can be directly calculated by Bragg's Law, then the in-plane strain states ( $\varepsilon_{x,\text{buffer}}$ ,  $\varepsilon_{x,\text{AlN:Si}}$ ) can be evaluated by assuming a biaxially strained layer and taking the elastic constants of AlN into account. It's worth noticing that  $\varepsilon_{x,\text{Si:AlN}}$  only represents the strain state of the Si:AlN top interface, not the averaged strain state of the bulk AlN:Si. The estimated dislocation densities of the buffer, the regrown Si:AlN thicknesses, the strain states of both layers are summarized in Table I. Detailed strain states and TDD of every layers can be found in supporting information.  $\varepsilon_{x,\text{buffer}}$  exhibits compressive strain ranging from -0.260% to -0.293%, which stems from the thermal mismatch between sapphire and AlN [42]. The density of threading dislocations with an edge component ( $\rho_e$ ) was two orders of magnitude higher than that of those with a screw component ( $\rho_s$ ). Hence, the strain-related phenomena in this report are dominated by pure edge TDs. The  $\varepsilon_{x,\text{Si:AlN}}$  is strongly dependent on both the initial edge TDD from the buffer ( $\rho_{e,\text{buffer}}$ ) and the thickness  $h$  of the re-

**Table I**

Summary of the buffer threading dislocation densities (TDD), in-plane strain states of the buffer ( $\varepsilon_{x,\text{buffer}}$ ), regrowth thickness ( $h$ ), and in-plane strain states of the top interface of the Si:AlN layer ( $\varepsilon_{x,\text{AlN:Si}}$ ).

| Sample | TDD ( $\times 10^8 \text{ cm}^{-2}$ ) |          | $\varepsilon_{x,\text{buffer}}$ (%) | $h$ ( $\mu\text{m}$ ) | $\varepsilon_{x,\text{AlN:Si}}$ (%) |
|--------|---------------------------------------|----------|-------------------------------------|-----------------------|-------------------------------------|
|        | $\rho_s$                              | $\rho_e$ |                                     |                       |                                     |
| A-1    | 0.14                                  | 4.91     | -0.286                              | 3.45                  | -0.179                              |
| A-2    | 0.09                                  | 5.78     | -0.291                              |                       | -0.165                              |
| A-3    | 0.04                                  | 6.72     | -0.277                              |                       | -0.059                              |
| A-4    | 0.09                                  | 8.04     | -0.274                              |                       | -0.059                              |
| A-5    | 0.19                                  | 8.91     | -0.293                              |                       | -0.056                              |
| A-6    | 0.14                                  | 10.16    | -0.284                              |                       | -0.001                              |
| B-1    | 0.03                                  | 7.67     | -0.271                              | 1.61                  | -0.178                              |
| B-2    | 0.01                                  | 7.58     | -0.269                              | 2.18                  | -0.138                              |
| B-3    | 0.08                                  | 8.02     | -0.260                              | 2.42                  | -0.112                              |
| B-4    | 0.02                                  | 9.53     | -0.269                              | 2.66                  | -0.079                              |
| B-5    | 0.02                                  | 10.20    | -0.260                              | 2.99                  | -0.019                              |
| B-6    | 0.09                                  | 7.59     | -0.265                              | 3.45                  | -0.014                              |
| B-7    | 0.02                                  | 8.26     | -0.274                              | 3.56                  | 0.009                               |

grown AlN:Si. The higher the  $\rho_{e,\text{buffer}}$ , the more efficient the compressive strain is relaxed. Similarly, the thicker the regrown AlN:Si, the less compressive is the film. In samples A-6 and B-7, the strain state of the Si:AlN top interface is like that of free-standing bulk AlN ( $\varepsilon_{x,\text{AlN:Si}} \sim 0$ ) or slightly tensile ( $\varepsilon_{x,\text{AlN:Si}} > 0$ ). Considering that the thermal expansion coefficient of sapphire is higher than that of AlN, the strain states at growth temperature were more tensile than those values measured at room temperature. The gradual change of the strain state with thickness implies that the lattice constant of the AlN template can be actively controlled by the thickness of the Si:AlN layer from compressive to tensile strain state.

To quantitatively model the strain states, we define the in-plane strain state variation of the AlN by ( $f_{\text{AlN}}$ ) by:

$$f_{\text{AlN}} = \varepsilon_{x,\text{AlN:Si}} - \varepsilon_{x,\text{buffer}}, \quad (1)$$

and the gradient of the in-plane strain along the [001] direction ( $\dot{\varepsilon}$ ) by:

$$\dot{\varepsilon} = \frac{d\varepsilon_x}{dz} = \frac{f_{\text{AlN}}}{h} \quad (2)$$

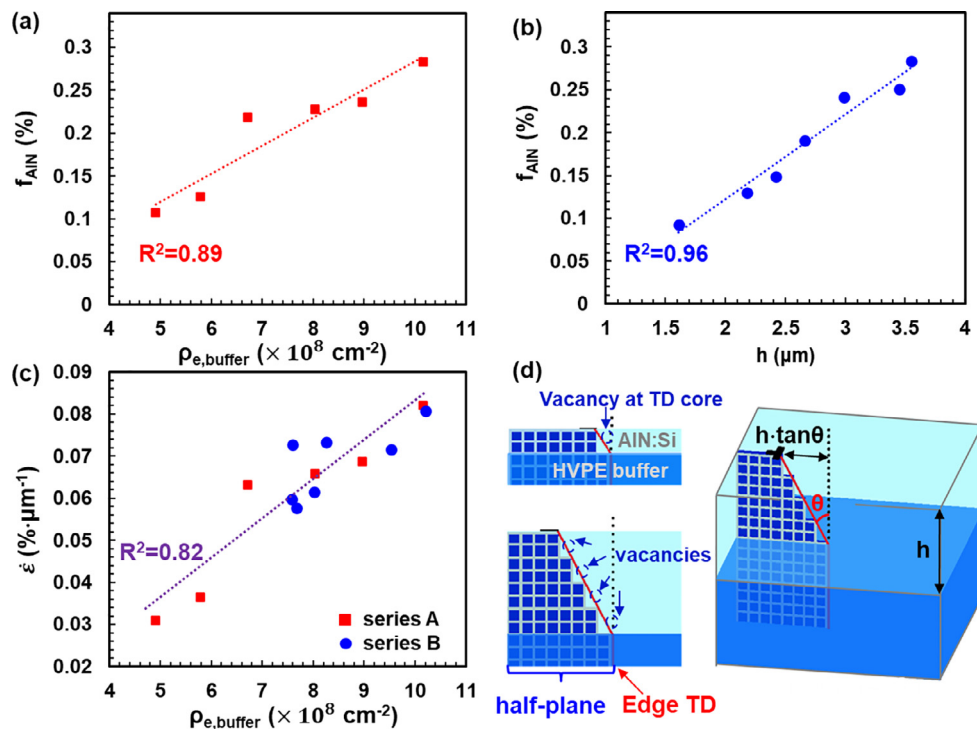


**Fig. 2.** The in-plane strain variation ( $f_{\text{AlN}}$ ) versus (a) initial edge TDD of buffer ( $\rho_{e,\text{buffer}}$ ) of series A (b) Si:AlN thickness ( $h$ ) of series B. (c) The in-plane strain gradient along  $c$ -axis vs.  $\rho_{e,\text{buffer}}$  of all samples. Dashed line is the linear regression with  $R^2$  values marked beside it. (d) Schematic illustration of vacancy-mediated dislocation inclination in AlN:Si.

In Fig. 2(a)  $f_{\text{AlN}}$  vs.  $\rho_{e,\text{buffer}}$  of series A is plotted while in 2(b)  $f_{\text{AlN}}$  vs.  $h$  of series B, and in 2(c)  $\dot{\varepsilon}$  vs.  $\rho_{e,\text{buffer}}$  of all samples is shown. The trends are in good agreement with a simple linear fit passing through the origin. The equation for the linear fit can be written after combining (1) and (2):

$$f_{\text{AlN}} = \varepsilon_{x,\text{AlN:Si}} - \varepsilon_{x,\text{buffer}} = \dot{\varepsilon}h \quad (3)$$

According to Fig. 2(c), we can write:

$$\dot{\varepsilon} = A\rho_{e,\text{buffer}}, \quad (4)$$

while  $A$  is a proportional constant, which was estimated to be  $8.1 \times 10^{-2} \text{ nm}$  by regression. Following that, the strain states of the Si:AlN top interface can be modeled by:

$$\varepsilon_{x,\text{AlN:Si}} = \varepsilon_{x,\text{buffer}} + A\rho_{e,\text{buffer}}h \quad (5)$$

In this study, the in-plane strain varied up to 0.3% in the Si:AlN layer. In other words, the in-plane lattice constant of the AlN template was expanded by up to 0.3% of its nature value. This mismatch is equivalent to the mismatch between freestanding  $\text{Al}_{0.88}\text{Ga}_{0.12}\text{N}$  and AlN. The reduction of 0.3% in compressive strain is crucial for growing a micrometer thick AlGaN with Al content <65%. As long as the Si:AlN film does not crack due to the increasing amount of tensile strain, the engineerable range of the lattice constant can be further extended.

The physical mechanism of the lattice-engineerable AlN template is illustrated in Fig. 2(d). As aforementioned, the carrier density of Al-rich n-AlGaN is strongly limited by vacancy compensation. The higher the Al content, the higher the concentration of vacancies. Every edge TD is attached to an extra half-plane in the AlN epitaxial film. When a vacancy interacts with the core of an edge TD, the half-plane withdraws one atom near the growth front. As the film grows, the accumulated atomistic recess results in the mesoscopic dislocation inclination. The extra half-planes shorten  $h \cdot \tan\theta$ , as depicted in Fig. 2(d), where  $\theta$  is the inclination angle

of the edge TD from the surface normal. Therefore, the average in-plane lattice constant of AlN is widened due to the reduced effective number of planes in the same area. This vacancy-mediated dislocation tilt was proposed and observed on n-GaN and n-AlGaN [43,44]. However, noticeable strain relaxation only occurred in n-GaN with a very high TDD ( $> 1 \times 10^{10} \text{ cm}^{-2}$ ) [43]. This might be explained by a lower tendency for vacancy formation in n-GaN. Dislocation tilt and bending were commonly observed in n-AlGaN, but they are not only driven by the vacancy-TD interaction, but also lattice mismatch strain between AlGaN and AlN. Therefore, it is difficult to decouple the parallel mechanisms and predict the final strain state by structure design.

According to the mechanical model by A. Romanov and J. Speck, the strain evolution with TD inclination can be written as [45]

$$\varepsilon_{x,\text{top}} = \varepsilon_{x,\text{bottom}} + \frac{1}{2}b \cdot \tan\theta \cdot \rho_e h \quad (6)$$

where  $\varepsilon_{x,\text{top}}/\varepsilon_{x,\text{bottom}}$  is the strain state of top/bottom interface of the epitaxial film,  $\rho_e$  is the edge dislocation density, and  $\mathbf{b}$  is the magnitude of the Burgers vector of the edge TD. For AlN,  $\mathbf{b} = \mathbf{a} = 0.3111 \text{ nm}$ . The  $1/2$  originates from the equal probability of half-plane shortening in orthogonal directions. In comparison with Eq. (5), we obtain  $A = \frac{1}{2}b \cdot \tan\theta = 8.1 \times 10^{-2} \text{ nm}$ , which gives  $\tan\theta = 0.521$  and  $\theta = 27.5^\circ$ .

To verify Eq. (6), we conducted cross-sectional transmission electron microscopy (TEM) to observe the actual TD inclination angle in AlN:Si. Without knowing the exact orientation of the TD inclination, two TEM samples were fabricated along both a-axis [110] and m-axis [100] by focused ion beam preparation. The exact-zone dark field (DF) images of the a-axis sample and the m-axis sample are shown in Fig. 3(a) and (b), respectively. The type of dislocations (edge, screw or mixed) was further confirmed by weak-beam dark-field images (not shown here). The edge dislocations in either Fig. 3(a) and (b) can be categorized into three groups according to the inclination angle: (1) high-tilt TDs marked in red

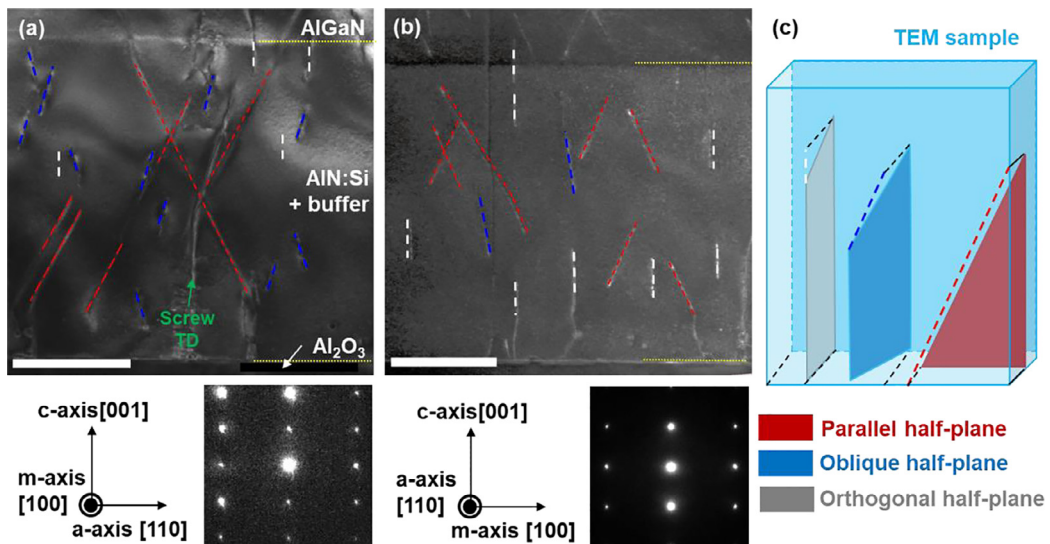


**Fig. 3.** Exact-zone DF TEM image on samples cut along (a) a-axis [110] direction (b) m-axis [100] direction of the wurtzite crystal. The orientation and diffraction patterns are written below the DF image. The white scale bars at the corner represents 1  $\mu\text{m}$  length. (c) Schematic illustration of the relative orientation between TEM sample, extra half-plane, and projected TD line.

**Table II**  
Summary of average inclination angles in Fig. 3.

| $\theta(^{\circ})$ | sample // a | sample // m | of both |
|--------------------|-------------|-------------|---------|
| High-tilt TD       | 27.8        | 25.5        | 26.4    |
| Low-tilt TD        | 15.9        | 9.4         | 14.9    |

(2) low-tilt TDs marked in blue, and (3) orthogonal TDs marked in white. The averaged  $\theta$  of high/low-tilt TDs are summarized in Table II.

The relative geometric orientation between the shortening half-planes and the TEM sample is illustrated in Fig. 3(c). If the half-plane is parallel to the TEM sample, the edge TD projection to the TEM sample would exhibit the largest  $\theta$  and the longest length. Therefore, the inclination angle of high-tilt TDs shall best reflect the real inclination angle of TDs in the solid. On the other hand, if the extra half-plane is orthogonal to the TEM sample, the TD projection only yields a short vertical segment. Since the orthogonal TDs were observed on both samples, the TD inclination could be either toward the a-axis or the m-axis. The low-tilt TDs suggest the half-plane is oblique to the TEM samples. The currently available information is not sufficient to determine the detailed structure. It might be TDs inclining towards oblique a-axis and m-axis, or more complex structures as revealed in n-GaN [42]. Since the vacancy-mediated TD inclination is a mesoscopic phenomenon of probabilistic half-plane recess, the inclination angle is not a deterministic value in the crystal. If we average  $\theta$ 's of the 13 high-tilt TDs from Fig. 3, the result is  $\theta=26.4^{\circ}$ , which is in good agreement with the value extracted from Fig. 2(c) and Eq. (6) ( $\theta=27.5^{\circ}$ ).

### 3.2. Optimal dislocation density for thick ALGaN/AlN heteroepitaxy

XRD  $\omega$ -scans were conducted on the Si:AlN and n-AlGaN layers to monitor the evolution of  $\rho_e$  and  $\rho_s$  through the subsequent epitaxial layers. The dependence of the TDD in Si:AlN ( $\rho_{e,\text{AlN:Si}}$ ,  $\rho_{s,\text{AlN:Si}}$ ) and n-AlGaN ( $\rho_{e,\text{AlGaN}}$ ,  $\rho_{s,\text{AlGaN}}$ ) on  $\rho_{e,\text{buffer}}$  is plotted in Fig. 4(a) and (b); that of  $\rho_{e,\text{AlGaN}}$  and  $\rho_{s,\text{AlGaN}}$  on  $\varepsilon_{x,\text{buffer}}$  is plotted in Fig. 4(c) and (d), respectively. From Fig. 4(a), the crystal quality was well transferred from the buffer to the regrown Si:AlN layer. The slightly lower TDD can be attributed to the pair annihilation of edge TDs with opposite burgers vectors during regrowth.

However, the good quality of AlN was not necessarily transferred to the subsequently grown n-AlGaN. For  $\rho_{e,\text{buffer}} > 8 \times 10^8 \text{ cm}^{-2}$ , the  $\rho_{e,\text{AlGaN}}$  is still close to the  $\rho_{e,\text{buffer}}$ . However, as  $\rho_{e,\text{buffer}}$  reduces to a lower value, the final  $\rho_{e,\text{AlGaN}}$  starts to deviate from it. In sample A-1, the final  $\rho_{e,\text{AlGaN}}$  rises to  $2 \times 10^9 \text{ cm}^{-2}$ , which is four times higher than that of its buffer ( $\rho_{e,\text{buffer}} = 4.9 \times 10^8 \text{ cm}^{-2}$ ). Therefore, the excess TDs are ascribed to new ones nucleated during n-AlGaN growth. From Fig. 4(b) and (d),  $\rho_s$  in Si:AlN and AlGaN ranges from  $8.1 \times 10^7 \text{ cm}^{-2}$  to  $3.4 \times 10^8 \text{ cm}^{-2}$ , which is 10 to 100 times higher than  $\rho_{s,\text{buffer}}$  in Table I. Therefore, the dislocations with a screw component in Si:AlN and AlGaN are unlikely the extension of original screw dislocations in the buffer. In the AlGaN/AlN epitaxial system, strain can also be relaxed via prismatic gliding along the  $(10\bar{1}1)$  plane. The prismatic gliding will produce misfit dislocations (MDs) at the AlGaN/AlN interface, which are attached to a mixed TD as described in reference [46]. Under a higher compressive strain, more pure edge TDs will be rendered into mixed TDs with MDs for strain relaxation. This explains why  $\rho_s$  is higher for samples with the lowest  $\rho_{e,\text{buffer}}$  (A-1 and A-2) and the least h (B-1). According to Eq. (5) and Fig. 4(d), the Si:AlN top interface of A-1, A-2 and B-1 were the most compressive ones. In particular,  $\rho_{s,\text{AlGaN}}$  of A-1 approached  $\rho_{e,\text{buffer}}$ , which implies most of pre-existing edge TDs have evolved into mixed TDs. Since the number of pre-existing TDs was insufficient to accommodate the compressive strain, nucleation of new TDs became inevitable. In practice, the rising  $\rho_{s,\text{AlGaN}}$  can be regarded as a warning sign of AlGaN epilayer instability in terms of relaxation by nucleation of new TDs.

Therefore, for a given thickness and composition of an AlGaN layer, an “optimal” initial edge dislocation density ( $\rho_{e,\text{opt}}$ ) exists. If  $\rho_{e,\text{buffer}} > \rho_{e,\text{opt}}$ , the IQE will be low due to the high TDD from the buffer; if  $\rho_{e,\text{buffer}} < \rho_{e,\text{opt}}$ , the IQE might eventually still be low due to the critical nucleation of new TDs during n-AlGaN growth. In this study, the  $\rho_{e,\text{opt}}$  for 1.6  $\mu\text{m}$   $\text{Al}_{0.63}\text{Ga}_{0.37}\text{N}$  was within  $7.0 \times 10^8 \text{ cm}^{-2}$  to  $8.0 \times 10^8 \text{ cm}^{-2}$  while the final  $\rho_{e,\text{AlGaN}}$  was in the same range. Fig. 5 shows the reciprocal space maps (RSM) of samples A-1 and B-1. We extracted the strain states of each layer based on their coordinates ( $Q_x, Q_z$ ) in the 114 RSM plot. (See supporting information) The in-plane strain variation during AlGaN growth ( $f_{\text{AlGaN}}$ ) is defined by:

$$f_{\text{AlGaN}} = \varepsilon_{x,\text{AlGaN}}^f - \varepsilon_{x,\text{AlGaN}}^i \quad (7)$$

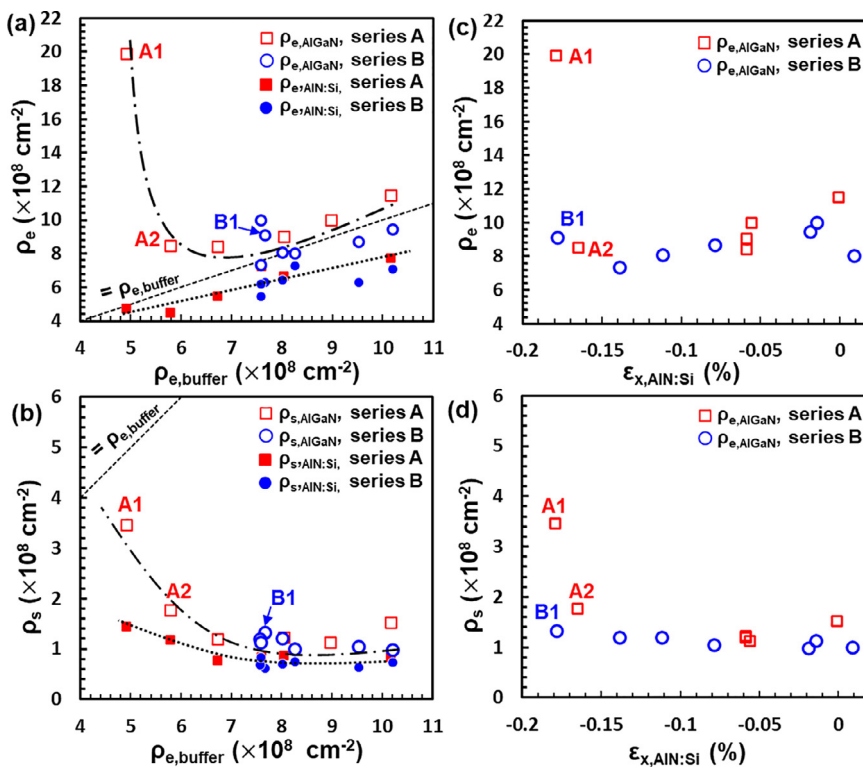


**Fig. 4.** Dependence of (a) edge and (b) screw dislocation densities of Si:AlN and n-AlGaN on the initial edge dislocation density from the buffer layer. Dashed lines in figure (a) and (b) are guides to the eye to highlight the trends. The dependence of (c) edge and (d) screw dislocation densities of n-AlGaN on the strain state of the Si:AlN top interface. AlGaN data points of specific samples (A1, A2, and B1) are directly marked in the figures.

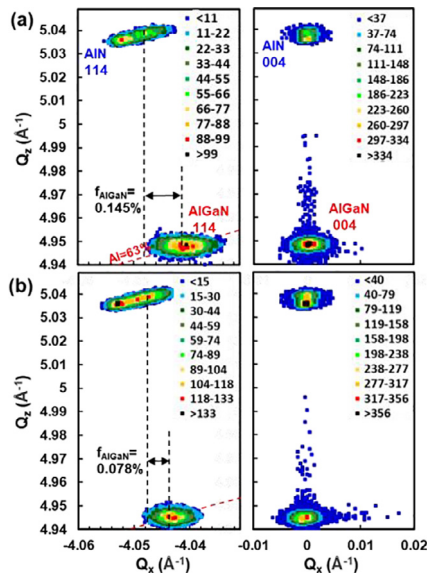


**Fig. 5.** X-ray RSM plot of 114 (left) and 004 (right) reflection of sample (a) B1 and (b) A1.

where  $\varepsilon_{x,\text{AlGaN}}^f$  is the strain state evaluated from the present AlGaN peak in the RSM plots and  $\varepsilon_{x,\text{AlGaN}}^i$  is the initial strain state assuming  $Q_{x,\text{AlGaN}} = Q_{x,\text{AlN:Si}}$ . It turns out that  $f_{\text{AlGaN}}$  is 0.078% in A-1 and 0.145% in B-1. According to Table I, the  $\varepsilon_{x,\text{AlN:Si}}$  between A-1 and B-1 was close, and so was  $\varepsilon_{x,\text{AlGaN}}^i$  ( $-1.048\% \pm 0.002\%$ ). Therefore, the significantly higher  $\rho_{e,\text{AlGaN}}$  in A-1 cannot be attributed to the absolute value of lattice mismatch to the Si:AlN template. The higher  $f_{\text{AlGaN}}$  indicates that the compressive strain is better accom-

modated with a higher initial edge TDD in B-1, so the critical TD nucleation was prevented during n-AlGaN epitaxy.

### 3.3. High power UVC LED with a low forward voltage

Finally, full LED growth was performed on a B-7-like n-AlGaN/Si:AlN structure with  $\rho_{e,\text{buffer}} \sim 7.0 \times 10^8 \text{ cm}^{-2}$ . According to the theoretical model [21], such TDD shall give a 16–20% IQE. The photographs of the on-wafer quick-test and a chip operating under  $I = 1000 \text{ mA}$  are shown in Fig. 6(a). The L-I-V, EQE, WPE, and electroluminescence (EL) characteristics curves are summarized in Fig. 6(b)–(d). Under standard operation condition of  $I = 350 \text{ mA}$ , the output power is  $P = 60 \text{ mW}$ , which yields an EQE of 3.8%. The UVC LEDs demonstrate a remarkably low forward voltage of  $V_f = 5.2 \text{ V}$  under  $I = 350 \text{ mA}$ . The corresponding WPE is 3.4%. Due to the suppressed Joule-heating, the LED shows low droop in both EQE and WPE under high current injection. When  $I = 1350 \text{ mA}$ , we observed  $P = 212 \text{ mW}$  while  $V_f = 5.7 \text{ V}$ . Under these conditions the EQE and WPE was still 3.5% and 2.8%, respectively, while the dynamic resistance was only  $0.4 \Omega$ . The superior electrical characteristics is not only attributed to the decent electrical contacts on the p-GaN and n-AlGaN, but also the low sheet resistance due to a moderate Al content and decent thickness of the n-AlGaN layer. Another evidence of low self-heating is the stable EL characteristics with rising injection current density ( $J$ ). The peak wavelength was around 275.8 nm and FWHM was 10.1 nm under low current injection. The peak wavelength and FWHM variation were all within 0.3 nm from  $J = 20 \text{ A}\cdot\text{cm}^{-2}$  to  $135 \text{ A}\cdot\text{cm}^{-2}$ . Although the absolute EQE values are still below the benchmark due to the limited LEE with the p-GaN/ITO contact scheme, the capability of high current injection makes it a practical choice for sterilization applications which requires a high absolute power density.

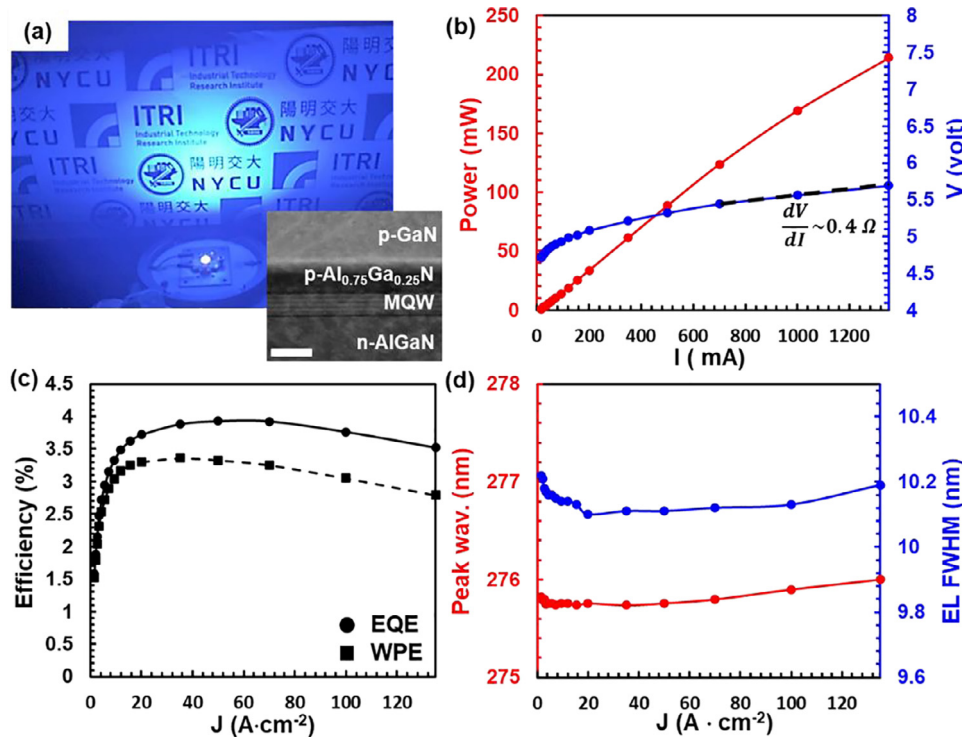


**Fig. 6.** (a) The upper image is a photograph of a packaged flip-chip under  $I = 1000$  mA injection. The lower image is the TEM image of LED near its active region. The white bar represents 50 nm. The LED heterostructure epilayers faced down and the probes were buried in the bottom. (b) L-I-V curves (c) EQE and WPE curves (d) EL peak wavelength and FWHM vs. current density ( $J$ ) for selected LED chips.

#### 4. Conclusion

In conclusion, we revealed the difficulty in fabricating a n-AlGaN current spreading layers simultaneously with a moderate Al content (<65%), a low TDD ( $<1 \times 10^9 \text{ cm}^{-2}$ ), and a sufficient thickness ( $>1.5 \mu\text{m}$ ) in UVC LEDs. The pre-existing edge dislocations play a dual role in the n-AlGaN epitaxy. Although edge TDs act as non-radiative centers in the active region, they also delay dislocation nucleation induced by the high compressive strain. Therefore, an optimal range for the initial edge dislocation density ( $\rho_{e,\text{opt}}$ ) of the buffer exists. To lower the limit of  $\rho_{e,\text{opt}}$ , we introduced high Si-doping in the AlN template to engineer its final in-plane lattice constant. As long as the strain state and the edge dislocation density of the buffer are given, the final strain state of the Si:AlN can be manipulated by the regrowth thickness. The top in-plane lattice constant of AlN can be increased until layer cracking. On top of a slightly tensile Si:AlN template, UVC LEDs with a  $1.6 \mu\text{m}$  thick n-Al<sub>0.63</sub>Ga<sub>0.37</sub>N spreading layer and final  $\rho_{e,\text{AlGaN}} \sim 7.0 \times 10^8 \text{ cm}^{-2}$  were fabricated. For any targeted thickness and composition of the n-AlGaN spreading layer, the  $\rho_{e,\text{opt}}$  can be deduced systematically with the methodology presented in this report. Finally, we demonstrated a high-power ( $>200$  mW) UVC LED chip, which could operate under  $J > 100 \text{ A} \cdot \text{cm}^{-2}$  while keeping a low  $V_f < 5.8 \text{ V}$ . This AlGaN strain-engineering development methodology with Si:AlN templates is expected to boost the performance of future UVB/UVC LEDs, especially for those which require a relatively higher amount of Ga in the device epitaxy.

#### Declaration of Competing Interest

The authors declare no conflict of interest.

#### Acknowledgment

The authors would like to thank SCIOCS Ltd. Japan for their professional and generous support in supplying high-quality HVPE

buffer layers. This work was partially supported by the German Federal Ministry of Education and Research (BMBF) through the consortium “Advanced UV for Life” under project contract 03ZZ0134B. This work was partly supported by the Higher Education Sprout Project of the National Yang Ming Chiao Tung University and Ministry of Education (MOE), Taiwan.

#### Supplementary materials

Supplementary material associated with this article can be found, in the online version, at doi:[10.1016/j.actamat.2022.117625](https://doi.org/10.1016/j.actamat.2022.117625).

#### References

- [1] A. Khan, K. Balakrishnan, T. Katona, Ultraviolet light-emitting diodes based on group three nitrides, *Nat. Photonics* 2 (2008) 77–84.
- [2] D. Li, K. Jiang, X. Sun, C. Guo, AlGaN photonics: recent advances in materials and ultraviolet devices, *Adv. Opt. Photonics* 10 (10) (2018) 43–110.
- [3] M. Kneissl, T. Seong, J. Han, H. Amano, The emergence and prospects of deep-ultraviolet light-emitting diode technologies, *Nat. Photonics* 13 (2019) 233–244.
- [4] H. Amano, R. Collazo, C. De Santi, S. Einfeldt, M. Funato, J. Glaab, S. Hagedorn, A. Hirano, H. Hirayama, R. Ishi, Y. Kashima, Y. Kawakami, R. Kirste, M. Kneissl, R. Martin, F. Mehnke, M. Meneghini, A. Ougazzaden, P.J. Parbrook, S. Rajan, P. Reddy, F. Römer, J. Ruschel, B. Sarkar, F. Scholz, L.J. Schowalter, P. Shields, Z. Sitar, L. Sulmoni, T. Wang, T. Wernicke, M. Weyers, B. Witzigmann, Y.-R. Wu, T. Wunderer, Y. Zhang, The 2020 UV emitter roadmap, *J. Phys. D Appl. Phys.* 53 (2020) 503001.
- [5] A.M. Armani, D.E. Hurt, D. Hwang, M.C. McCarthy, A. Scholtz, Low-tech solutions for the COVID-19 supply chain crisis, *Nat. Rev. Mater.* 5 (2020) 403–406.
- [6] A.C.K. Lai, S.S. Nunayon, A new UVC-LED system for disinfection of pathogens generated by toilet flushing, *Indoor Air* 31 (2020) 324–334.
- [7] L. Shen, T.M. Griffith, P.O. Nyangaresi, Y. Qin, X. Pang, G. Chen, M. Li, Y. Lu, B. Zhang, Efficacy of UVC-LED in water disinfection on bacillus species with consideration of antibiotic resistance issue, *J. Hazard. Mater.* 386 (2020) 121968.
- [8] F.A. Juarez-Leon, A.G. Soriano-Sánchez, M.A. Rodríguez-Licea, F.J. Perez-Pinal, Design and implementation of a germicidal UVC-LED lamp, *IEEE Access* 8 (2020) 196951–196962.
- [9] M. Bormann, M. Alt, L. Schipper, L. van de Sand, M. Otte, T.L. Meister, U. Dittmer, O. Witzke, E. Steinmann, A. Krawczyk, Disinfection of SARS-CoV-2 contaminated surfaces of personal items with UVC-LED disinfection boxes, *Viruses* 13 (2021) 598.

- [10] S. Liu, W. Luo, D. Li, Y. Yuan, W. Tong, J. Kang, Y. Wang, D. Li, X. Rong, T. Wang, Z. Chen, Y. Li, H. Wang, W. Wang, J. Hoo, L. Yan, S. Guo, B. Shen, Z. Cong, X. Wang, Sec-eliminating the SARS-CoV-2 by AlGaN based high power deep ultraviolet light source, *Adv. Funct. Mater.* 31 (2021) 2008452.
- [11] T. Takano, T. Mino, J. Sakai, N. Noguchi, K. Tsubaki, H. Hirayama, Deep-ultraviolet light-emitting diodes with external quantum efficiency higher than 20% at 275nm achieved by improving light-extraction efficiency, *Appl. Phys. Express* 10 (2017) 031002.
- [12] M. Shatalov, W. Sun, A. Lunev, X. Hu, A. Dobrinsky, Y. Bilenko, J. Yang, M. Shur, R. Gaska, C. Moe, AlGaN deep-ultraviolet light-emitting diodes with external quantum efficiency above 10%, *Appl. Phys. Express* 5 (2012) 082101.
- [13] M.A. Khan, N. Maeda, M. Jo, Y. Akamatsu, R. Tanabe, Y. Yamada, H. Hirayama, 13mW operation of a 295–310nm AlGaN UV-B LED with a p-AlGaN transparent contact layer for real world applications, *J. Mater. Chem. C* 7 (2019) 143–152.
- [14] N. Maeda, M. Jo, H. Hirayama, Improving the efficiency of AlGaN Deep-UV LEDs by using highly reflective Ni/Al p-type electrodes, *Phys. Status Solidi A* 215 (2018) 1700435.
- [15] H.K. Cho, N. Susilo, M. Guttmann, J. Rass, I. Ostermay, S. Hagedorn, E. Ziffer, T. Wernicke, S. Einfeldt, M. Weyers, M. Kneissl, Enhanced wall plug efficiency of AlGaN-based deep-UV LEDs using Mo/Al as p-contact, *IEEE Photonics Technol. Lett.* 32 (2020) 891–894.
- [16] C.Y. Huang, C.L. Tsai, C.Y. Huang, R.Y. Yang, Y.C. Sermon Wu, H.W. Yen, Y.K. Fu, Efficiency improvement analysis of nano-patterned sapphire substrates and semi-transparent superlattice contact layer in UVC light-emitting diodes, *Appl. Phys. Lett.* 117 (2020) 261102.
- [17] S.R. Lee, A.M. West, A.A. Allerman, K.E. Waldrip, D.M. Follstaedt, P.P. Provencio, D.D. Koleske, C.R. Abernathy, Effect of threading dislocations on the Bragg peakwidths of GaN, AlGaN, and AlN heterolayers, *Appl. Phys. Lett.* 86 (2005) 241904.
- [18] R. Chierchia, T. Böttcher, H. Heinke, S. Einfeldt, S. Figge, D. Hommel, Microstructure of heteroepitaxial GaN revealed by x-ray diffraction, *Appl. Phys. Lett.* 93 (2003) 8918.
- [19] K. Moszak, W. Olszewski, D. Pucicki, J. Serafińczuk, K. Opołczyńska, M. Rudziński, R. Kudrawiec, D. Hommel, Verification of threading dislocations density estimation methods suitable for efficient structural characterization of Al<sub>x</sub>Ga<sub>1-x</sub>N/GaN heterostructures grown by MOVPE, *Appl. Phys. Lett.* 126 (2019) 165304.
- [20] N. Susilo, E. Ziffer, S. Hagedorn, L. Cancellara, C. Netzel, N.L. Ploch, S. Wu, J. Rass, S. Walde, L. Sulmoni, M. Guttmann, T. Wernicke, M. Albrecht, M. Weyers, M. Kneissl, Improved performance of UVC-LEDs by combination of high-temperature annealing and epitaxially laterally overgrown AlN/sapphire, *Photonics Res.* 8 (2020) 589–594.
- [21] K. Ban, J. Yamamoto, K. Takeda, K. Ide, M. Iwaya, T. Takeuchi, S. Kamiyama, I. Akasaki, H. Amano, Internal quantum efficiency of whole-composition-range AlGaN multiquantum wells, *Appl. Phys. Express* 4 (2011) 052101.
- [22] J. Bai, M. Dudley, W.H. Sun, H.M. Wang, M.Asif Khan, Reduction of threading dislocation densities in AlN/sapphire epilayers driven by growth mode modification, *Appl. Phys. Lett.* 88 (2006) 051903.
- [23] P. Dong, J. Yan, Y. Zhang, J. Wang, J. Zeng, C. Geng, P. Cong, L. Sun, T. Wei, L. Zhao, Q. Yan, C. He, Z. Qin, J. Li, AlGaN-based deep ultraviolet light-emitting diodes grown on nano-patterned sapphire substrates with significant improvement in internal quantum efficiency, *J. Cryst. Growth* 395 (2014) 9–13.
- [24] I. Demir, H. Li, Y. Robin, R. Mc Clintock, S. Elagoz, M. Razeghi, Sandwich method to grow high quality AlN by MOCVD, *J. Phys. D Appl. Phys.* 51 (2018) 085104.
- [25] L. Zhang, F. Xu, J. Wang, C. He, W. Guo, M. Wang, B. Sheng, L. Lu, Z. Qin, X. Wang, B. Shen, High-quality AlN epitaxy on nano-patterned sapphire substrates prepared by nano-imprint lithography, *Sci. Rep.* 6 (2016) 35934.
- [26] S. Xiao, N. Jiang, K. Shojiki, K. Uesugi, H. Miyake, Preparation of high-quality thick AlN layer on nanopatterned sapphire substrates with sputter-deposited annealed AlN film by hydride vapor-phase epitaxy, *Jpn. J. Appl. Phys.* 58 (2019) SC1003.
- [27] H. Fujikura, T. Konno, T. Kimura, H. Miyake, AlN nanostructures and flat, void-less AlN templates formed by hydride vapor phase epitaxy on patterned sapphire substrates, *Appl. Phys. Express* 13 (2020) 025506.
- [28] B. Tang, H. Hu, H. Wan, J. Zhao, L. Gong, Y. Lei, Q. Zhao, S. Zhou, Growth of high-quality AlN films on sapphire substrate by introducing voids through growth-mode modification, *Appl. Surf. Sci.* 518 (2020) 146218.
- [29] H. Miyake, C.-H. Lin, K. Tokoro, K. Hiramatsu, Preparation of high-quality AlN on sapphire by high-temperature face-to-face annealing, *J. Cryst. Growth* 456 (2016) 155–159.
- [30] C.Y. Huang, P.Y. Wu, K.S. Chang, Y.H. Lin, W.C. Peng, Y.Y. Chang, J.P. Li, H.W. Yen, Y.C. Sermon Wu, H. Miyake, H.C. Kuo, High-quality and highly-transparent AlN template on annealed sputter-deposited AlN buffer layer for deep ultra-violet light-emitting diodes, *AIP Adv.* 7 (2017) 055110.
- [31] R. Yoshizawa, H. Miyake, K. Hiramatsu, Effect of thermal annealing on AlN films grown on sputtered AlN templates by metalorganic vapor phase epitaxy, *J. Jpn. Appl. Phys.* 57 (2018) 01AD05.
- [32] D. Wang, K. Uesugi, S. Xiao, K. Norimatsu, H. Miyake, Low dislocation density AlN on sapphire prepared by double sputtering and annealing, *Appl. Phys. Express* 13 (2020) 095501.
- [33] Y. Iba, K. Shojiki, K. Uesugi, S. Xiao, H. Miyake, MOVPE growth of AlN films on nano-patterned sapphire substrates with annealed sputtered AlN, *J. Cryst. Growth* 532 (2020) 125397.
- [34] D.V. Dinh, N. Hu, Y. Honda, H. Amano, M. Pristovsek, High-temperature thermal annealing of nonpolar (1010) AlN layers sputtered on (1010) sapphire, *J. Cryst. Growth* 498 (2018) 377–380.
- [35] L. Chen, W. Lin, H. Chen, H. Xu, C. Guo, Z. Liu, J. Yan, J. Sun, H. Liu, J. Wu, W. Guo, J. Kang, Annihilation and regeneration of defects in (1122) semipolar AlN via high-temperature annealing and MOVPE regrowth, *J. Ye, Cryst. Growth Des.* 21 (2021) 2911–2919.
- [36] N. Susilo, S. Hagedorn, D. Jaeger, H. Miyake, U. Zeimer, C. Reich, B. Neuschuz, L. Sulmoni, M. Guttmann, F. Mehnke, C. Kuhn, T. Wernicke, M. Weyers, M. Kneissl, AlGaN-based deep UV LEDs grown on sputtered and high temperature annealed AlN/sapphire, *Appl. Phys. Lett.* 112 (2018) 041110.
- [37] J.S. Harris, J.N. Baker, B.E. Gaddy, I. Bryan, Z. Bryan, K.J. Mirrieles, P. Reddy, R. Collazo, Z. Sitar, D.L. Irving, On compensation in Si-doped AlN, *Appl. Phys. Lett.* 112 (2018) 152101.
- [38] K. Kataoka, T. Narita, K. Nagata, H. Makino, Y. Saito, Electronic degeneracy conduction in highly Si-doped Al<sub>0.6</sub>Ga<sub>0.4</sub>N layers based on the carrier compensation effect, *Appl. Phys. Lett.* 117 (2020) 262103.
- [39] I. Bryan, Z. Bryan, S. Washiyama, P. Reddy, B. Gaddy, B. Sarkar, M.H. Breckinridge, Q. Guo, M. Bobea, J. Tweedie, S. Mita, D. Irvin, R. Collazo, Z. Sitar, Doping and compensation in Al-rich Al<sub>0.55</sub>Ga<sub>0.45</sub>N films grown on single crystal AlN and sapphire by MOCVD, *Appl. Phys. Lett.* 112 (2018) 062102.
- [40] Y. Kawase, S. Ikeda, Y. Sakuragi, S. Yasue, S. Iwayama, M. Iwaya, T. Takeuchi, S. Kamiyama, I. Akasaki, H. Miyake, Ultraviolet-B band lasers fabricated on highly relaxed thick Al<sub>0.55</sub>Ga<sub>0.45</sub>N films grown on various types of AlN wafers, *Jpn. J. Appl. Phys.* 58 (2019) SC1052.
- [41] C.Y. Huang, S. Walde, C.L. Tsai, C. Netzel, H.H. Liu, S. Hagedorn, Y.R. Wu, Y.K. Fu, M. Weyers, Overcoming the excessive compressive strain in AlGaN epitaxy by introducing high Si-doping in AlN templates, *Jpn. J. Appl. Phys.* 59 (2020) 070904.
- [42] M.X. Wang, F.J. Xu, N. Xie, Y.H. Sun, B.Y. Liu, W.K. Ge, X.N. Kang, Z.X. Qin, X.L. Yang, X.Q. Wang, B. Shen, High-temperature annealing induced evolution of strain in AlN epitaxial films grown on sapphire substrates, *Appl. Phys. Lett.* 114 (2019) 112105.
- [43] J. Xie, S. Mita, A. Rice, J. Tweedie, L. Hussey, R. Collazo, Z. Sitar, Strain in Si doped GaN and the fermi level effect, *Appl. Phys. Lett.* 98 (2011) 202101.
- [44] J. Weinrich, A. Mogilatenko, F. Brunner, C.T. Koch, M. Weyers, Extra half-plane shortening of dislocations as an origin of tensile strain in Si-doped (Al)GaN, *Appl. Phys. Lett.* 126 (2019) 085701.
- [45] A.E. Romanov, J.S. Speck, Stress relaxation in mismatched layers due to threading dislocation inclination, *Appl. Phys. Lett.* 83 (2003) 2569.
- [46] Z. Wu, K. Nonaka, Y. Kawai, T. Asai, F.A. Ponce, C. Chen, M. Iwaya, S. Kamiyama, H. Amano, I. Akasaki, Strain relaxation mechanisms in AlGaN epitaxy on AlN templates, *Appl. Phys. Express* 3 (2010) 111003.